

Article

Synthesis of Novel Ternary Dual Z-scheme AgBr/LaNiO₃/g-C₃N₄ Composite with Boosted Visible-Light Photodegradation of Norfloxacin

Junjiao Zhang ¹, Zhengru Zhu ¹, Junchao Jiang ^{1,*} and Hong Li ²

¹ School of Geography, Liaoning Normal University, Dalian 116029, China; zjjcaihong@outlook.com (J.Z.); zhengruzhu@lnnu.edu.cn (Z.Z.)

² Department of Basic, Dalian Naval Academy, Dalian 116018, China; lswlx903@163.com

* Correspondence: jiangjunchao@lnnu.edu.cn; Tel.: +86-411-8215-8364

Received: 18 July 2020; Accepted: 13 August 2020; Published: 14 August 2020



Abstract: Promoting the separation of photogenerated charges and enhanced optical absorption capacity is the main means to modify photocatalytic capacities to advance semiconductor photocatalyst applications. For the first time, a novel ternary photocatalyst for dual Z-scheme system AgBr/LaNiO₃/g-C₃N₄ (ALG) was prepared via a modest ultrasound-assisted hydrothermal method. The results indicated that LaNiO₃ nanoballs and AgBr nanoparticles were successfully grown on the surface of g-C₃N₄ nanosheets. A dual Z-scheme photocatalytic reaction system could be constructed based on the energy band matching within AgBr, LaNiO₃ and g-C₃N₄. Metallic Ag during the photocatalytic reaction process acted as the active electrons transfer center to enhance the photocatalytic charge pairs separation. The chemical composition of ALG was optimized and composites with 3% AgBr, 30% LaNiO₃ and 100% g-C₃N₄ which was noted as 3-ALG displayed the best photocatalytic performance. A total of 92% of norfloxacin (NOR) was photodegraded within two hours over ALG and the photodegradation rate remained >90% after six cycles. The main active species during the degradation course were photogenerated holes, superoxide radical anion and hydroxyl radical. A possible mechanism was proposed based on the synergetic effects within AgBr, LaNiO₃ and g-C₃N₄. This work would offer a credible theoretical basis for the application of dual Z-scheme photocatalysts in environment restoration.

Keywords: g-C₃N₄; dual Z-scheme; ternary photocatalyst; norfloxacin; photocatalysis

1. Introduction

In previous decades, antibiotics were widely used for the treatment and prevention of bacterial infections in human and animal healthcare. A large number of antibiotic wastewater is discharged into the environment without appreciating treatment [1]. Especially the fluoroquinolone antibiotic, norfloxacin (NOR), which was extensively used as a therapeutic and prophylactic antimicrobial agent in clinical medical treatment, aquaculture, and animal husbandry [2]. NOR has been detected in rivers, lakes and ground water [3]. The continuous accumulation of NOR can damage the security and stability of the natural environment.

Numerous researches had found that semiconductor photocatalytic technology can be efficacious means of solving the growing environmental pollution and energy crisis around the world [4–7]. However, common photocatalyst are limited in application for narrow light absorption range, poor stabilization, and lower photodegradation efficiency [8,9]. To improve the photocatalytic performance, abundant research was carried out concentrating on the formation of Z-scheme heterojunction [10,11], especially dual Z-scheme system photocatalyst [12]. In the course of a photocatalytic reaction over

a dual Z-scheme photocatalyst, benefited from the nice matching of energy bands, photogenerated charge pairs are effectively separated, transferred. Finally the reaction center could be formed due to the accumulation of conduction band (CB) and valence band (VB) to remove the organic pollution in water.

Nowadays, $g\text{-C}_3\text{N}_4$ has a great application prospect for removal of organic contamination from water [13]. It has the advantages of controllable, inexpensive synthesis, and stable chemical properties [14,15]. But wide band gap and high charge recombination were the shortcoming of $g\text{-C}_3\text{N}_4$. It still needs essential improvement. For the improvement of this situation and to make it more suitable for practical application, it needs to be modified and compounded with other activated materials, especially establishing the dual Z-scheme system photocatalyst according to the energy bands matching of related materials.

Perovskite structure semiconductor possesses excellent performance in fuel cells, catalytic combustion, conductive materials, and photocatalysis [16,17]. Among them, a p-type semiconductor, LaNiO_3 , has promising applications in the field of photodegradation of organic contaminants and in hydrogen production benefitting from suitable band gap and electronic magnetic property. Many photocatalytic composites were successfully prepared, such as $\text{LaNiO}_3/\text{ZnIn}_2\text{S}_4$ [18], $\text{LaNiO}_3/\text{SnS}_2$ [19], $\text{LaNiO}_3/\text{CdS}$ [20] and $\text{LaNiO}_3/\text{TiO}_2$ [21], which have made some progress in hydrogen production, dye degradation and tetracycline hydrochloride removal. Besides, as a semiconductor material with good photosensitivity, silver bromide (AgBr) is easy to synthesize, possesses stable physical and chemical properties, a narrow band gap, and outstanding renewability [22,23]. What's more, numerous heterojunctions were synthesized based on AgBr according to previous researches such as $\text{AgPO}_3/\text{AgBr}/g\text{-C}_3\text{N}_4$ [24], $\text{BiOBr}/\text{AgBr}/\text{LaPO}_4$ [25], and $\text{AgBr}/p\text{-}g\text{-C}_3\text{N}_4$ [26]. Because AgBr possesses a narrow band gap, strong photosensitivity and high charge separation ability, also AgBr is easiest to produce metallic Ag under illumination, which can promote electron transfer in heterojunctions and improve charge separation efficiency. In addition, LaNiO_3 and AgBr have good energy band matching with $g\text{-C}_3\text{N}_4$, which is an excellent choice for the formation of a dual Z-scheme system over the heterojunction to promote photocatalytic reactions. However, the research concerning on dual Z-scheme reaction system over $\text{AgBr}/\text{LaNiO}_3/g\text{-C}_3\text{N}_4$ has not been reported until now to our knowledge.

Herein, $\text{AgBr}/\text{LaNiO}_3/g\text{-C}_3\text{N}_4$ (ALG) ternary component dual Z-scheme photocatalyst was prepared by an ultrasound-assisted hydrothermal method. The samples obtained were further characterized by XRD, FT-IR, XPS, SEM, TEM, DRS, BET, PL, EIS. We also examined the photodegradation of norfloxacin (NOR) under xenon lamp in aqueous solution over ALG. Benefiting from the energy band matching and activated materials modified, this ternary photocatalyst has remarkable optical absorption capacity and excellent photocatalytic decomposition of NOR. The intentionally constructed dual Z-scheme not only improves the separation of charge pairs but also provides more active species for photodegradation. A probable reaction mechanism within the dual Z-scheme over the photocatalyst was proposed depended on the relative energy bands of the three materials.

2. Results and Discussion

2.1. Microstructure and Surface Morphology

The crystal structures of samples were characterized using XRD and the patterns were depicted in Figure 1. It was obvious that the diffraction peaks of AgBr, $g\text{-C}_3\text{N}_4$, and LaNiO_3 as-prepared, were matched well with standard PDF card AgBr (JCPDS 64-38) [27], $g\text{-C}_3\text{N}_4$ (JCPDS 87-1526) [28], and LaNiO_3 (JCPDS 33-0711) [29], respectively. To be specific, the characteristic peaks of AgBr found at 26.92° , 31.01° , 44.39° , 52.66° , 55.18° , 64.58° , and 73.32° corresponded to (111), (200), (220), (311), (222) and (400) crystal faces, the diffraction peaks of $g\text{-C}_3\text{N}_4$ could be investigated at 13.02° and 27.56° which were attributed to (100) and (002) crystal planes. While those at 22.70° , 32.36° , 40.04° , 47.44° , 54.14° , 58.22° , 67.46° and 78.4° were assigned to (101), (110), (021), (202), (211), (122), (220) and (312)

lattice planes of LaNiO_3 . As revealed in Figure 1b, the diffraction peaks in Figure 1a can also be investigated in the patterns of Figure 1b. All the peak positions were well matched and no additional peaks appeared, which confirms the successful preparation of 30% $\text{LaNiO}_3/\text{g-C}_3\text{N}_4$ (LG) and ALG photocatalysts. The average crystalline sizes of all the samples could be calculated by the Scherrer equation [25], and the detailed data could be found in Table 1. The average crystalline sizes of AgBr and LaNiO_3 were 43.49 nm and 12.03 nm. The average crystalline size of x-ALG samples increase gradually from 20.56 to 26.47 nm because of the introduction of AgBr nanoparticles.

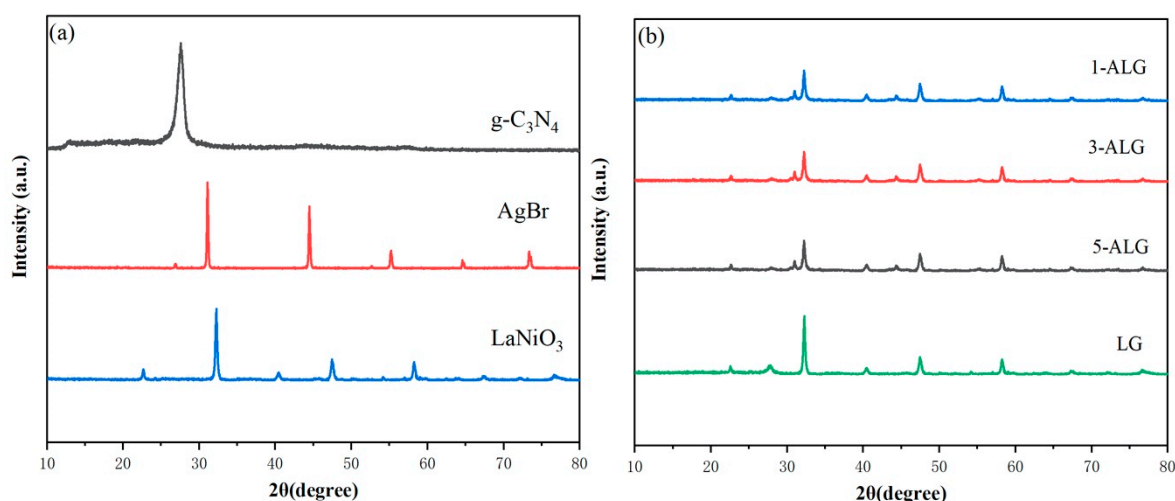


Figure 1. XRD patterns of bare $\text{g-C}_3\text{N}_4$, AgBr, LaNiO_3 (a), 1-ALG, 3-ALG and 5-ALG (b).

Table 1. The average pore sizes and specific surface areas of $\text{g-C}_3\text{N}_4$, 1-ALG, 3-ALG and 5-ALG.

| Sample Name | Average Pore Sizes (nm) | Specific Surface Areas (m^2/g) | Pore Volume (cm^3/g) | Crystalline Size (nm) |
|--------------------------|-------------------------|--|--|-----------------------|
| $\text{g-C}_3\text{N}_4$ | 27.99 | 27.32 | 0.78 | 2.57 |
| 1-ALG | 27.50 | 45.81 | 0.72 | 20.56 |
| 3-ALG | 26.19 | 65.39 | 0.64 | 25.68 |
| 5-ALG | 30.54 | 30.72 | 0.89 | 26.47 |

The vibrational features of functional groups existing in the samples were analyzed by FT-IR. The FT-IR spectra of AgBr, LG and ALG were depicted in Figure 2, consistent with $\text{g-C}_3\text{N}_4$, the sharp band discerned at 802 cm^{-1} represented the triazine units breathing mode [15]. The absorption bands ranging from $1207\text{--}1649\text{ cm}^{-1}$ corresponds to the vibration of C-N stretching modes [30]. The peaks are caused by the stretching vibrations of heptazine-derived repeating units. The wide band ranging from $3087\text{--}3395\text{ cm}^{-1}$ could be attributed to N-H vibration modes [31].

Because AgBr and LaNiO_3 were both inorganic materials and the stretching vibrations of them were hard to investigate by FT-IR. Based on this situation, TEM was employed to investigate the deposition of AgBr and LaNiO_3 on the surface of $\text{g-C}_3\text{N}_4$. The characteristic bands of absorption water was overlapped by the absorption bands of $\text{g-C}_3\text{N}_4$, and the existent of water could confirmed by XPS [32].

The elemental composition of 3-ALG was examined by XPS and displayed in Figure 3a including La, Ni, O, Ag, Br, C, and N, which agrees with the chemical constituents of ALG. In Figure 3b, two pairs of shoulder peaks at 837.74, 834.70 eV and 851.69, 855.21 eV represent La $3d_{5/2}$ and La $3d_{3/2}$ [17]. The peaks at 855.04 and 869.59 eV are assigned to Ni $2p_{3/2}$ and Ni $2p_{1/2}$, also the satellite peak appeared at 864.35 and 878.75 eV, as shown in Figure 3c, indicating that Ni valence is +3 [33]. As shown in Figure 3d, The peaks at 529.64 and 531.23 are attributed to lattice oxygen and the chemisorbed oxygen from absorption water [33]. In Figure 3e, the peaks at 284.80, 286.12, and 288.43 eV are attributed to

C-C coordination, sp^2 hybridized carbon, and sp^3 N-C=N group in $g-C_3N_4$. The N 1s spectrum is shown in Figure 3f, three peaks are fitted at 396.89, 398.95, and 402.54 eV, which are assigned to C-N=C, N-(C)₃ and N-H groups, respectively [12]. In Figure 3g, two peaks could be observed at 366.90 and 372.39 eV, which were assigned to Ag 3d_{5/2} and Ag 3d_{3/2} [23]. Br 3d spectrum in Figure 3h displayed two peaks at 68.23 and 69.52 eV which represent Br 3d_{5/2} and Br 3d_{3/2} [22]. The results investigated by XPS could confirm the successful synthesis of 3-ALG sample.

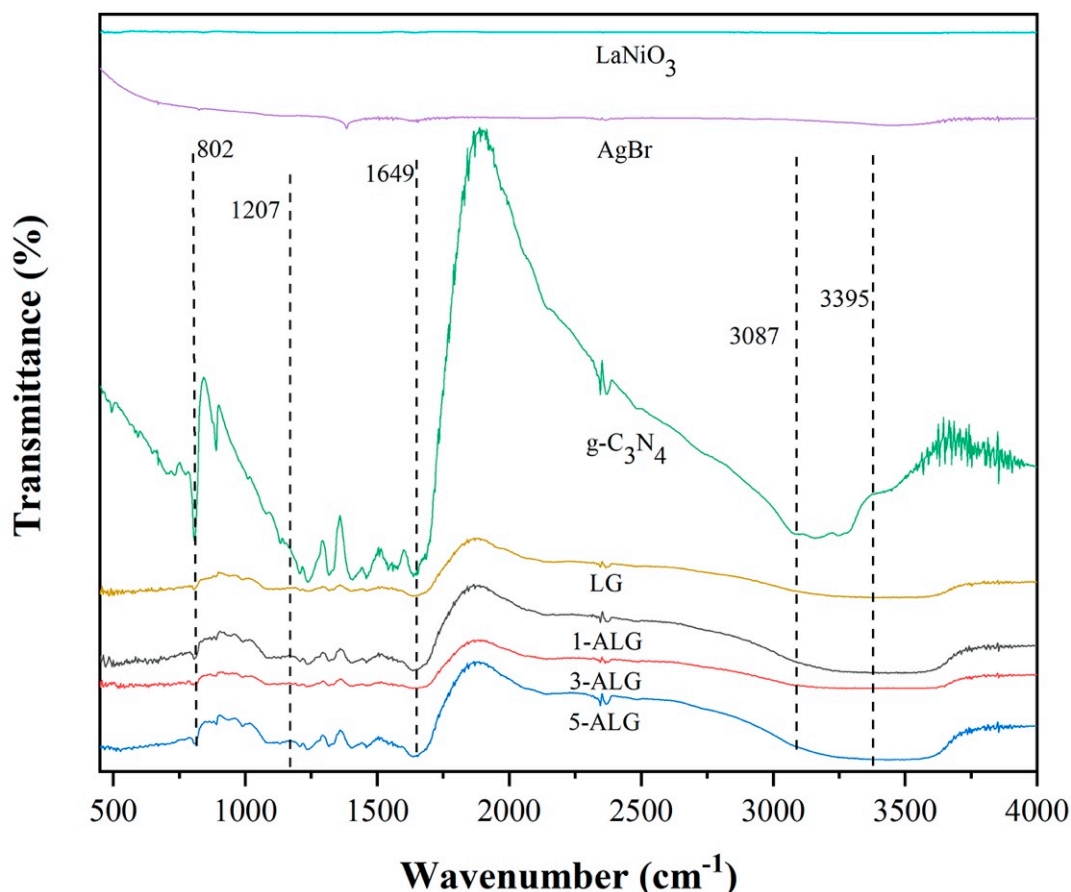


Figure 2. FT-IR spectra of bare AgBr, $g-C_3N_4$, 1-ALG, 3-ALG and 5-ALG.

To examine the surface microstructure and morphology, the morphological observation of AgBr, $LaNiO_3$, $g-C_3N_4$, LG and 3-ALG. The SEM and TEM images of samples were shown in Figure 4. In Figure 4a, AgBr displayed irregular-shaped nanoparticle structures with dimensions from 30–50 nm, which is consistent with the previously reported results. As examined in Figure 4b, $LaNiO_3$ exhibited nanosphere structures with a smooth surface and a diameter of about 60 nm. As observed in Figure 4c, $g-C_3N_4$ showed the aggregated and slightly transparent layered nanosheet structures, which is the typical surface morphology of $g-C_3N_4$ nanosheets. As displayed in Figure 4d, $LaNiO_3$ nanospheres were assembled with $g-C_3N_4$ indicating the formation of LG. After the addition of $LaNiO_3$ and AgBr (Figure 4e), we found that $LaNiO_3$ and AgBr were deposited on $g-C_3N_4$ nanosheets. The microstructure of 3-ALG was further characterized by TEM. The TEM result was shown in Figure 4f, in which darker $LaNiO_3$ and AgBr were evenly grown on the surface of $g-C_3N_4$ demonstrating the successful formation of ALG ternary component hybrid.

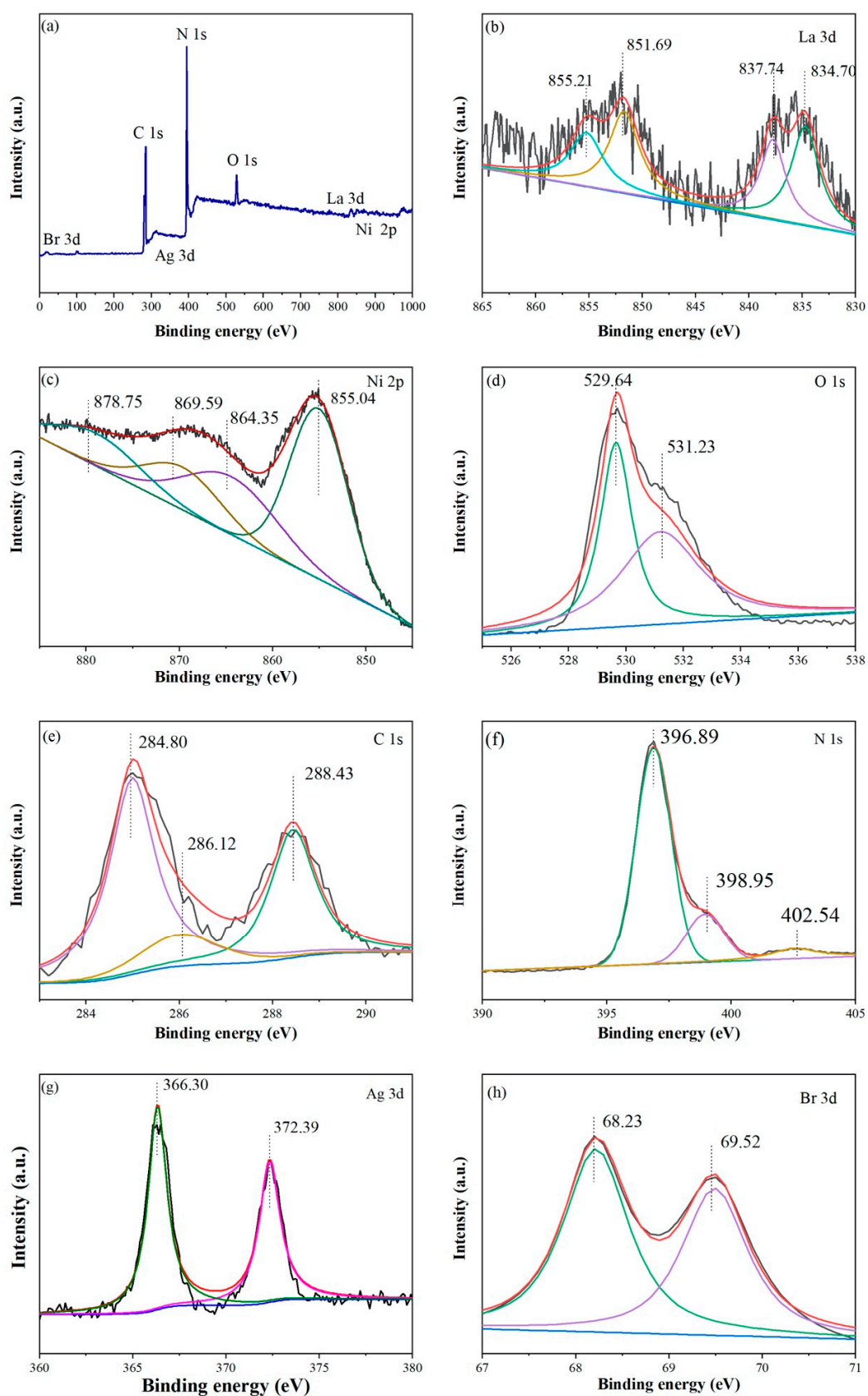


Figure 3. XPS spectra of as-obtained 3-ALG (a), La 3d (b), Ni 2p (c), O 1s (d), C 1s (e), N 1s (f), Ag 3d (g), and Br 3d (h).

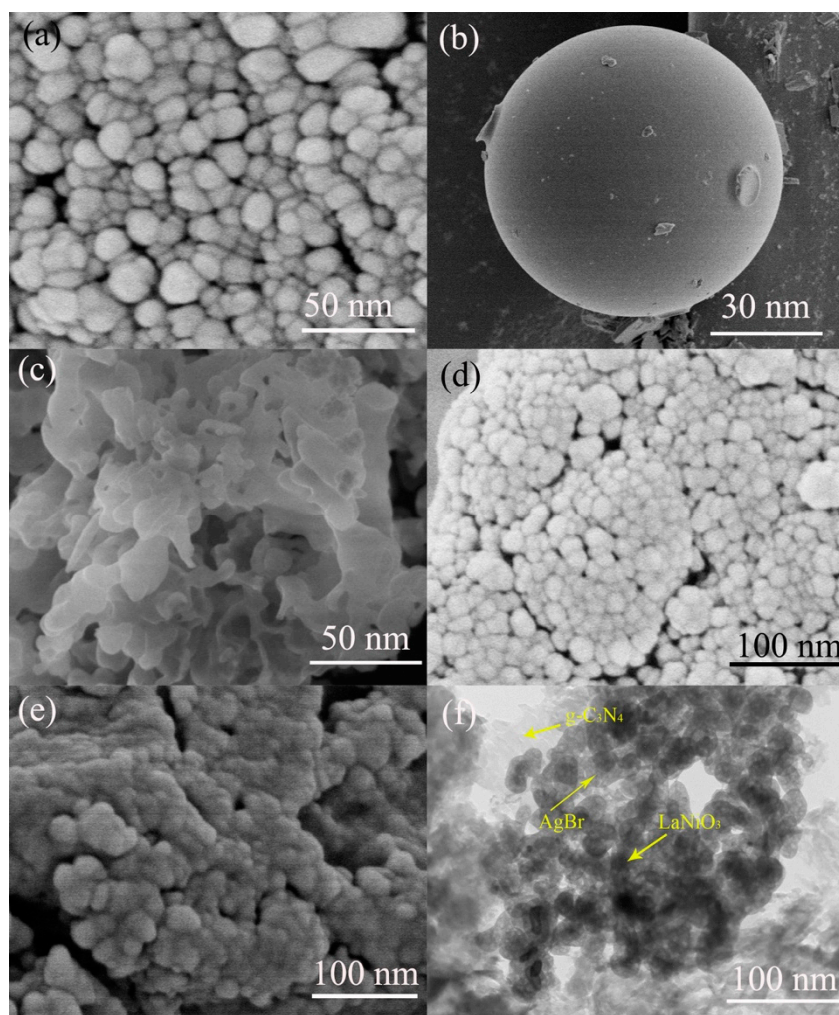


Figure 4. The SEM images of (a) AgBr, (b) LaNiO₃, (c) g-C₃N₄, (d) LG, (e) 3-ALG and TEM image of 3-ALG (f).

In order to examine the surface physico-chemical properties, the N₂ adsorption-desorption isotherms and corresponding pore size distribution were illustrated in Figure 5. As shown in Figure 5a, according to IUPAC classification, all the samples demonstrated type-IV isotherm with H₃ hysteresis loops, suggesting that all the samples presented typical mesoporous structure [33]. Among them, 3-ALG exhibited the highest adsorption isotherm, which demonstrates that sample 3-ALG possesses large pore size and tight intermolecular interactions of adsorbate molecules. The mesoporous structure of ALG composites and g-C₃N₄ was further proved by the plot of the pore-diameter distribution (Figure 5b) in which the average pore sizes of ALG composites and g-C₃N₄ were 27.99 nm (1-ALG), 27.50 nm (3-ALG), 26.19 nm (5-ALG) and 30.54 nm (g-C₃N₄) calculated by BJH model. The BET specific surface areas of g-C₃N₄ was shown in Table 1, which was calculated to be 27.32 m²/g. After coupling with AgBr and LaNiO₃, the BET specific surface areas increased from 45.81 to 65.39 m²/g and decreased to 30.72 m²/g. Because AgBr and LaNiO₃ were assembled on the g-C₃N₄ nanosheets by ultra-sonic treatment, more microvoids were appearing on the surface of g-C₃N₄ nanosheets, the BET specific areas increased first. When the superfluous LaNiO₃ was loaded on the surface of g-C₃N₄ nanosheets, partial pores of the hybrid were blocked leading to the decrease in the BET specific surface area. Generally, larger pore diameter and specific surface area are beneficial to the photocatalytic activity, which can adsorb more organics and increase the active sites for photocatalytic reaction.

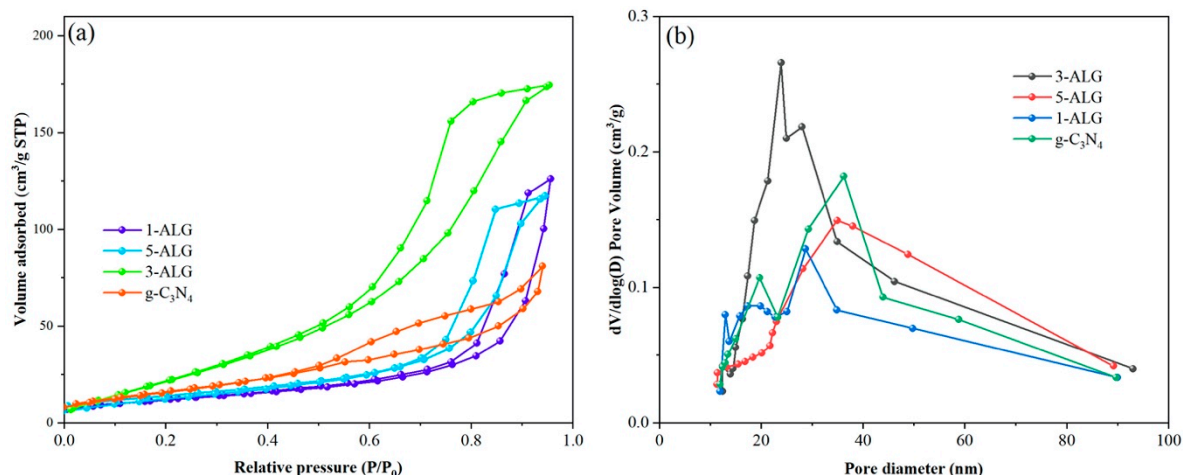


Figure 5. Nitrogen adsorption-desorption isotherms (a) and pore distribution curves (b) of bare $g-C_3N_4$ and 1-ALG, 3-ALG, and 5-ALG.

2.2. Optical Properties

The UV-Vis DRS was employed to analyze the light absorption capacities of obtained samples. The results were illustrated in Figure 6a. What could be observed is that all the samples examined could be excited by both visible light and UV light. It could also be seen that the absorption edges of $LaNiO_3$, $g-C_3N_4$, and AgBr were about 441, 488, and 500 nm. The sample LG showed stronger absorption than bare $g-C_3N_4$. The optical absorption edge of ALG exhibited redshift which gradually became larger with the increasing amount of AgBr. The band gaps of all the samples were estimated by the Tauc/David-Mott model [34]. The band gap value of bare $g-C_3N_4$ is 2.73 eV, after coupled with $LaNiO_3$ the value increased to 2.77 eV, furthermore, the band gap value became more smaller after the formation of ALG composites, the value of 5-ALG decreased to 2.70 eV even. Strong optical absorption capacity and narrow band gap are a benefit to the photocatalysis, so ALG hybrid will possess more enhanced photocatalytic performance than bare $g-C_3N_4$.

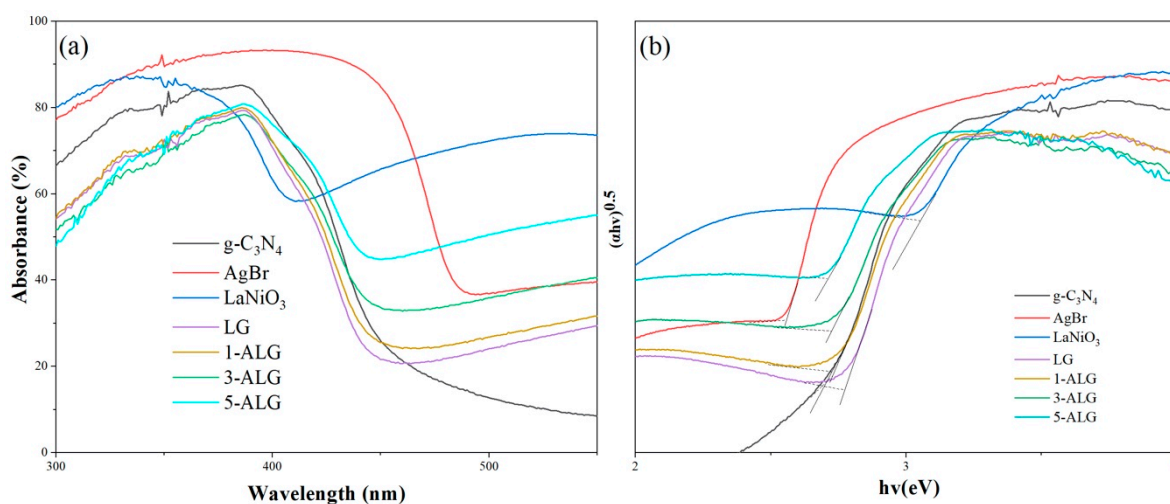


Figure 6. DRS spectra (a,b) the estimated band gap curves of all the samples obtained.

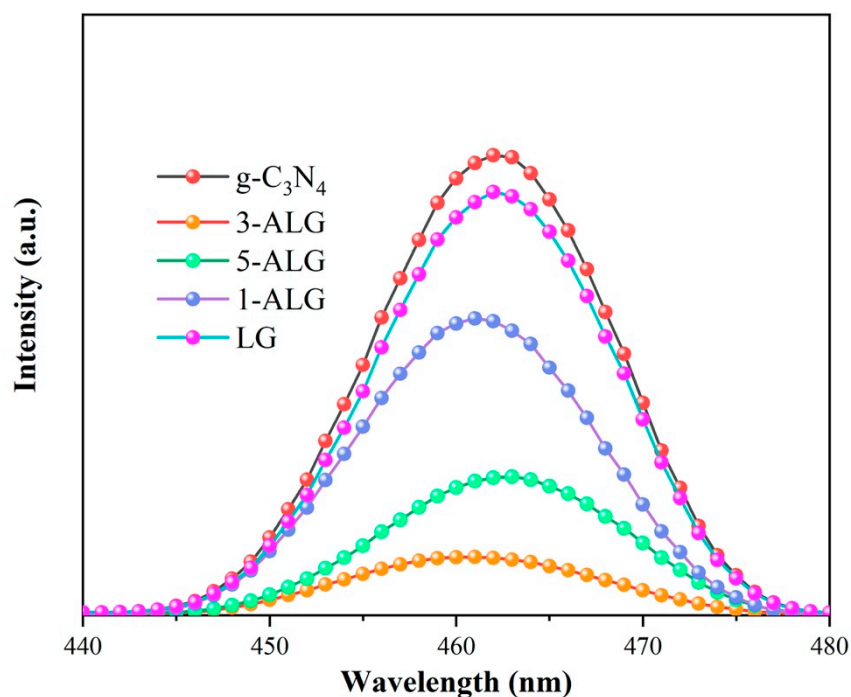
Meanwhile, the band edge positions of CB and VB of all the semiconductor obtained could be calculated by Tauc equation [15]. The calculated CB and VB were shown in the following Table 2.

Table 2. The band edge positions of conduction and valence band for the sample g-C₃N₄, AgBr and LaNiO₃ (pH = 7).

| Sample Name | CB (V vs. NHE) | VB (V vs. NHE) |
|---------------------------------|----------------|----------------|
| g-C ₃ N ₄ | −1.18 | 1.55 |
| AgBr | 0 | 2.55 |
| LaNiO ₃ | 0.23 | 3.23 |

Distinctly, the valence and conduction band potentials of LaNiO₃, AgBr, and g-C₃N₄ can be well-matched, making it possible to form a ternary component dual Z-scheme heterojunction composite photocatalyst, and the well-designed construction can suppress the recombination of photogenerated electrons and holes, promote the migration and transfer of photogenerated charge pairs, thereby enhancing the photocatalytic behavior.

The photoluminescence (PL) spectra were employed to investigate the photogenerated charge separation and migration in samples obtained by us with the excitation laser wavelength of 446 nm and the results were displayed in Figure 7. Generally, lower PL emission intensity represents lower recombination efficiency of photogenerated electrons and holes. As shown in Figure 7, the main emission peaks of g-C₃N₄ were located at around 460 nm, which was mentioned in the previous literature [15]. When compared with LG, 1-ALG, 3-ALG and 5-ALG, the PL peak intensity of g-C₃N₄ was stronger than them, and 3-ALG possessed the weakest PL intensity, which evidences that benefiting from the addition of LaNiO₃ and AgBr, LG and 3-ALG possessed better separation and migration efficiency of photogenerated electrons and holes than bare g-C₃N₄. Furthermore, the PL spectra explained the best photocatalytic performance of 3-ALG in all the samples obtained.

**Figure 7.** PL spectra of g-C₃N₄, LG, and 3-ALG.

The photocurrent response experiments of bare g-C₃N₄, LG and 3-ALG were employed to investigate the separation efficiency of photogenerated electrons and holes within the photocatalysts. As shown in Figure 8a, the transient photocurrent intensity of 3-ALG was much stronger than bare g-C₃N₄ and LG, which revealed that 3-ALG possessed the optimum separation efficiency for photo-aroused charge carriers. The migration and separation ability of photo-aroused electrons and holes within the samples was further investigated by the electrochemical impedance spectroscopy

(EIS). As illustrated in Figure 8b, it is apparent that the arc radius on the Nyquist plot of sample 3-ALG is distinctly smaller when compared with bare $g\text{-C}_3\text{N}_4$ and LG, indicating the lowest transfer resistance and highest separation efficiency of charge pairs.

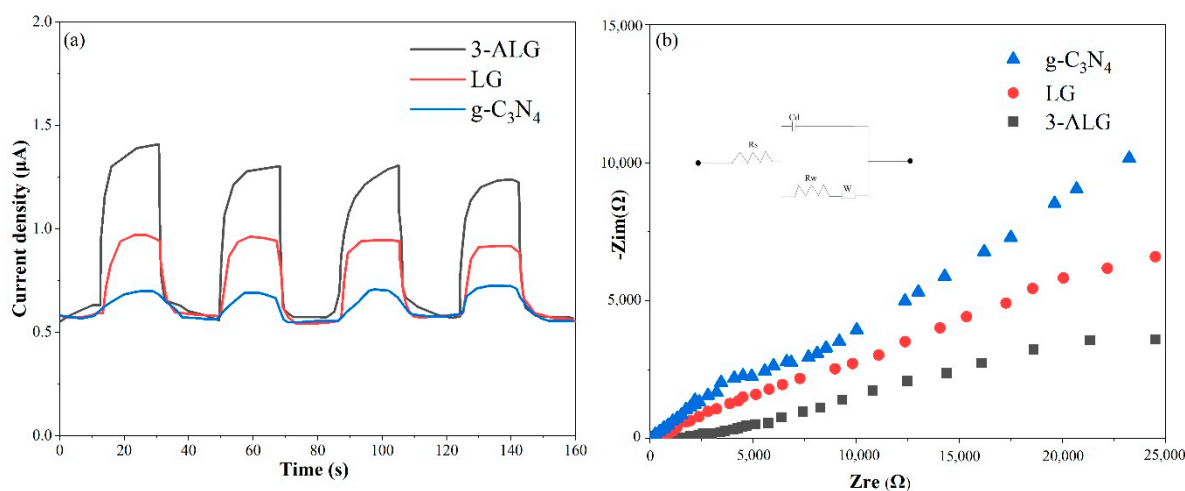


Figure 8. Photocurrent time curves (a) of $g\text{-C}_3\text{N}_4$, LG, and 3-ALG and EIS Nyquist plots (b).

In short, considering the results of PL, photocurrent, and EIS, we found that by the construction of the ALG ternary component heterojunction, the effective separation of photogenerated electrons and holes were achieved, which can provide more photoactive electrons and holes for subsequent photocatalytic reactions. The phenomena have a positive effect on enhancing the photocatalytic performance of the photocatalyst. The conclusion can be verified in subsequent degradation experiments.

2.3. Photocatalytic Activity

Norfloxacin (NOR) is a typical antibiotic, which is wide-used, colorless, odorless non-biodegradable, and commonly detected in wastewater. In order to compare the photocatalytic abilities of all the photocatalysts, the photocatalytic degradation experiment of NOR was implemented under visible light. After 40 min the adsorption-desorption equilibrium away from light was gained, and the curves of NOR degradation over all the photocatalysts were recorded and demonstrated in Figure 9a. As displayed in Figure 9a, there is almost no degradation without any photocatalysts in suspension. When with bare $g\text{-C}_3\text{N}_4$, AgBr, and LaNiO_3 , the degradation rates were still scant, reaching 40%, 38%, and 31%, respectively. While $g\text{-C}_3\text{N}_4$ coupled with LaNiO_3 , the photodegradation efficiency increased significantly, 80% of NOR was degraded within 120 min. The photocatalytic performance was enhanced further over the ternary component composite, the photocatalytic activities over ALG was 83% (1-ALG), 92% (3-ALG), and 87% (5-ALG). Obviously, the ternary component photocatalyst 3-ALG possesses the highest degradation ability towards NOR. The NOR photodegradation process was fitted by the pseudo-first-order kinetics. As displayed in Figure 9b and Table 3, the nice linear relationship between $-\ln(C_t/C_0)$ and t was gained using the model significantly. The apparent reaction rate constant of bare $g\text{-C}_3\text{N}_4$, AgBr, and LaNiO_3 were merely 0.00408, 0.00365 and 0.00299 min^{-1} , respectively. The degradation rate of NOR over LG hybrid was 0.01028 min^{-1} which is obviously faster than them. It is worth noting that all the ternary composite ALG showed the superior k value in which 3-ALG possessed the highest degradation rate of NOR up to 0.01790 min^{-1} . It is obvious that a significant improvement in catalytic performance can be achieved due to the addition of AgBr and LaNiO_3 on the surface of $g\text{-C}_3\text{N}_4$, which is benefited from the synergistic effect in the ternary heterojunction. The synergistic effect can inhibit the recombination of photogenerated holes and electrons, and promote the migration of photogenerated charge pairs. The photodegradation of NOR

under visible light irradiation prove that the photocatalytic ability of x-ALG were higher than bare g-C₃N₄, AgBr, LaNiO₃ as well as LG samples.

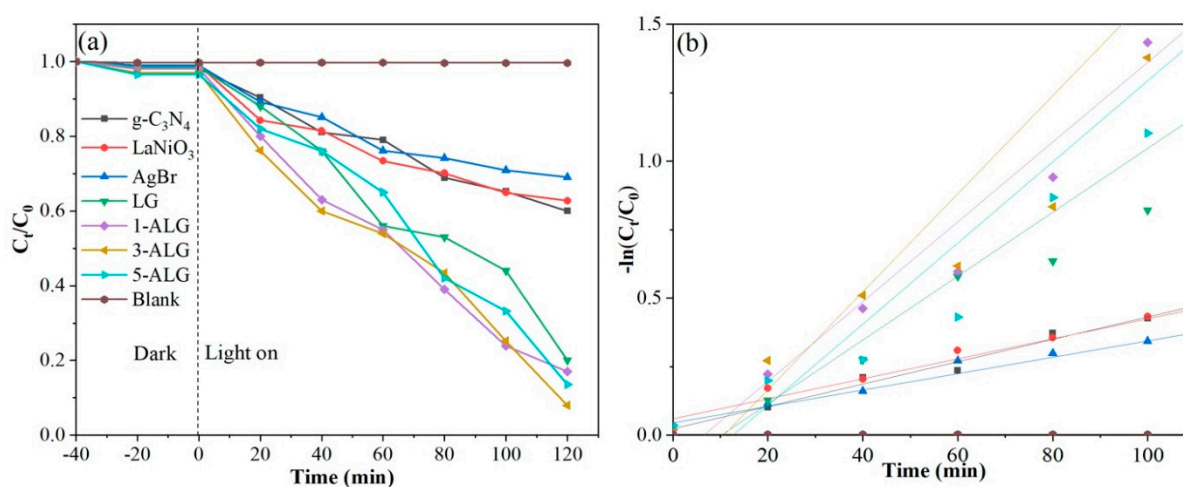


Figure 9. Photocatalytic performances (a) and the corresponding kinetic curves analyzed by the pseudo-first-order kinetic model (b) for NOR degradation over different photocatalysts.

Table 3. Photocatalytic results and crystalline size of all the samples.

| Sample Name | Degradation (%) | k (min ⁻¹) | Standard Deviation | Band Gap (eV) |
|---------------------------------|-----------------|--------------------------|--------------------|---------------|
| g-C ₃ N ₄ | 40 | 0.00408 | 0.01425 | 2.73 |
| AgBr | 31 | 0.00365 | 0.02134 | 2.55 |
| LaNiO ₃ | 38 | 0.00299 | 0.02348 | 3.00 |
| LG | 80 | 0.01166 | 0.14129 | 2.77 |
| 1-ALG | 83 | 0.01456 | 0.08799 | 2.73 |
| 3-ALG | 92 | 0.01790 | 0.24918 | 2.72 |
| 5-ALG | 87 | 0.01481 | 0.18515 | 2.70 |

In the actual application process, the photostability and reproducibility are essential for the photocatalyst. The recyclability study on 3-ALG was implemented, and the results were depicted in Figure 10a. 3-ALG was reused for four times, for each recycling experiment, 3-ALG was centrifuged from the suspension and washed with ethanol and distilled water for several times, and dried before the next recycle. As demonstrated in Figure 10b, it is not difficult that after four times recycle experiments, the catalytic performance of 3-ALG did not decline significantly, and 90% of NOR can still be degraded within two hours indicating the stability of 3-ALG. It can be confirmed by the XRD patterns of 3-ALG before and after the experiments. We found that there is no obvious contradiction can be detected, which further illustrated the reliability stability of 3-ALG in practical applications. In addition, we found two peaks at 38.21° and 43.6° which can be associated with (111) and (200) crystal plane of Ag (JCPDS 040783) [35], which could be attributed to the reduction of Ag⁺ to metal Ag during the photocatalytic process. The metal Ag can act as a transit center for photogenerated electrons, which is advantageous for the photocatalytic reaction.

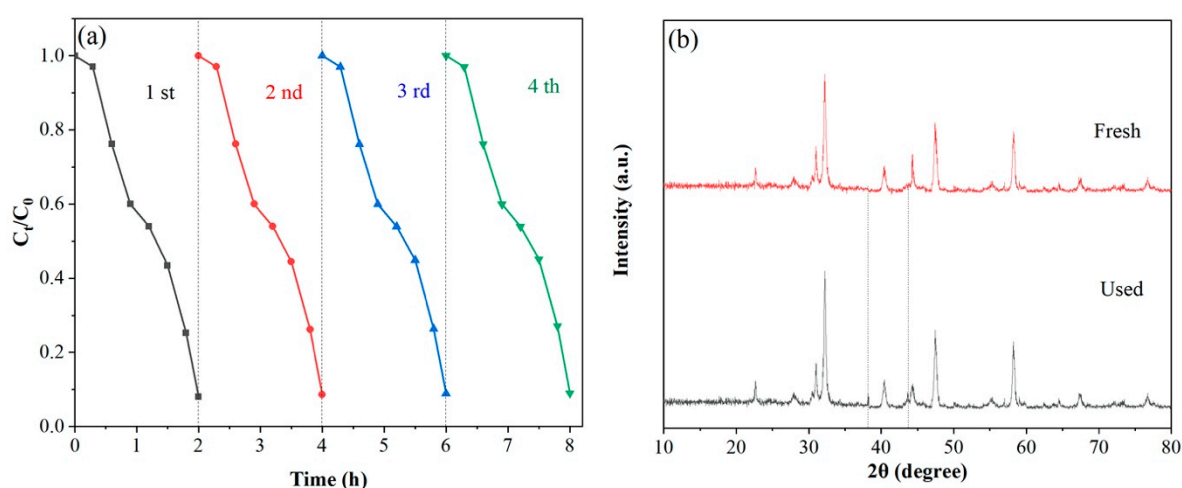


Figure 10. Recycling experiments (a) of the photocatalytic degradation of NOR over 3-ALG and (b) patterns of 3-ALG before and after sequential photocatalytic reaction under visible irradiation.

2.4. Photocatalytic Degradation of NOF Comparing with Other Materials

As an objective evaluation of our work, we compared the photocatalytic degradation of NOF over 3-ALG with other materials. According to the previous researches [4,36–39], $\text{FeVO}_4/\text{Fe}_2\text{TiO}_5$, $\text{CeO}_2/\text{g-C}_3\text{N}_4$, $\text{CoWO}_4/\text{g-C}_3\text{N}_4$, ZnS and $\text{BiWO}_4/\text{WO}_3$ were also taken and mixed with NOF aqueous solution under a 500 W xenon lamp equipped with a 420 nm cut filter for the degradation of NOF, which is as same as the degradation experiment over 3-ALG. As displayed in Table 4, apparently, the photocatalytic degradation of NOF over the materials demonstrated that the photocatalytic ability of 3-ALG under visible light illumination was at higher level.

Table 4. Photocatalytic degradation of 3-ALG, $\text{CeO}_2/\text{g-C}_3\text{N}_4$, ZnS, $\text{FeVO}_4/\text{Fe}_2\text{TiO}_5$, $\text{CoWO}_4/\text{g-C}_3\text{N}_4$ and $\text{BiWO}_4/\text{WO}_3$.

| Photocatalyst Name | Degradation Rate (%) | Photocatalyst Name | Degradation Rate (%) |
|---------------------------------------|----------------------|---|----------------------|
| 3-ALG | 92 | $\text{FeVO}_4/\text{Fe}_2\text{TiO}_5$ | 92 |
| $\text{CeO}_2/\text{g-C}_3\text{N}_4$ | 88.6 | $\text{CoWO}_4/\text{g-C}_3\text{N}_4$ | 97 |
| ZnS | 75 | $\text{BiWO}_4/\text{WO}_3$ | 67 |

2.5. Photocatalytic Mechanism

In order to analyze the significantly reinforced photocatalytic performance for NOR degradation over photocatalyst 3-ALG, the radical quenching experiments were conducted. Benzoquinone (BQ) as the scavenger for O_2^- , AgNO_3 for e^- , ethylenediaminetetraacetic acid disodium salt (EDTA-2Na) for h^+ , and isopropanol (IPA) for $\cdot\text{OH}$, were added to 3-ALG reaction system respectively. It is noteworthy that, although IPA can also react with h^+ and O_2^- , according to many previous literatures [40,41], the main trapping radical of IPA in the radical quenching experiment is OH. The experiment results were illustrated in Figure 11, the photocatalytic degradation efficiency of NOR was noticeably reduced when BQ, EDTA-2Na and IPA involved in the reaction system. There were only small changes in the reaction upon the introduction of AgNO_3 , which was because the activity of photogenerated electrons in the reaction is limited by addition of AgNO_3 , some of electrons in the CB were also limited to produce O_2^- , the same phenomenon appeared in the photocatalytic reaction system of $\text{BiFeO}_3/\text{ZrO}_2$ [42]. From the above phenomena, O_2^- , h^+ and OH can be identified as the main active species during the photodegradation process of NOR. Thus, the enhanced photocatalytic performance for NOR over ternary component dual Z-scheme heterojunction photocatalyst can be interpreted in terms of migration of photo-aroused charge pairs, the generation of h^+ and the corresponding radicals in aqueous solution.

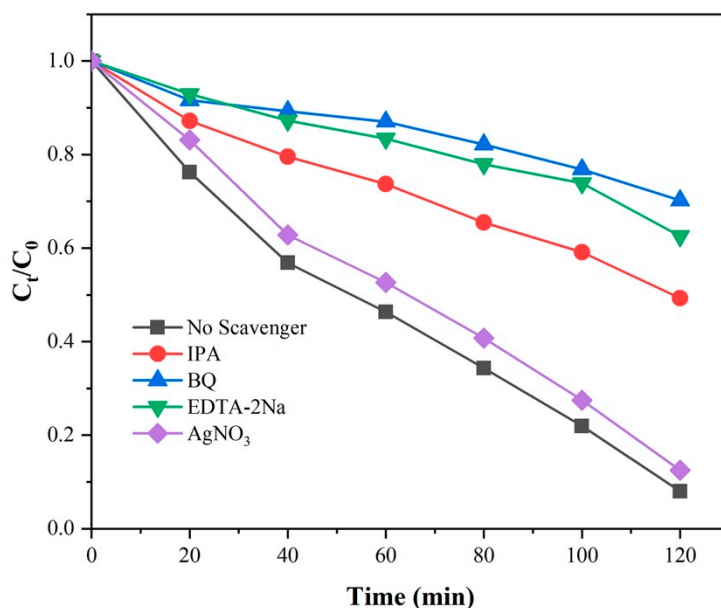


Figure 11. Radical quenching experiments over 3-ALG.

The powerful photocatalytic ability for NOR over 3-ALG under visible light was demonstrated by the photocatalytic experiments, and the main reactive species within the degradation system were clarified by the analysis of the radical quenching experiments. Therefore, a possible dual Z-scheme photocatalytic mechanism is proposed in Figure 12.

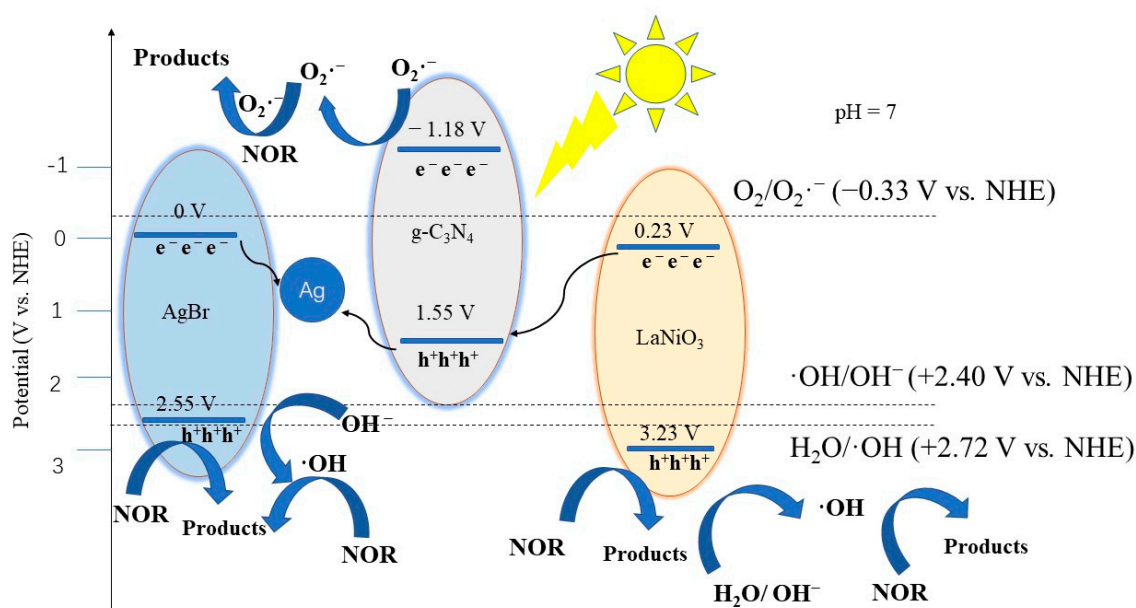


Figure 12. Proposed mechanism of as-prepared 3-ALG for the photocatalytic degradation of NOR under visible light irradiation (pH = 7).

As shown in Figure 12, in the photocatalytic degradation process, Ag^+ in AgBr is reduced to metallic Ag, moreover, metallic Ag can act as the photocatalytic charge pair transfer center of the dual Z-scheme. The e^- generated in the CB of AgBr can recombine with h^+ migrating from the VB of $\text{g-C}_3\text{N}_4$ on metallic Ag. Similarly, the e^- in the CB of LaNiO_3 can recombine with the h^+ in the VB of $\text{g-C}_3\text{N}_4$. By this means, a large number of photo-generated electrons are accumulated in the CB of $\text{g-C}_3\text{N}_4$, while plenty of positive holes (h^+) are retained in the VB of LaNiO_3 and AgBr, which resulted

in the efficacious separation of h^+ and e^- . Due to the CB potential of $g-C_3N_4$ is more negative than the potential O_2/O_2^- (-0.33 V vs. NHE at pH = 7), the e^- in the CB of $g-C_3N_4$ would reduce the O_2 dissolved in water into O_2^- . Meanwhile, the h^+ retained in the VB of $LaNiO_3$ and $AgBr$ could oxidize H_2O and OH^- to produce OH , because the VB potential of $AgBr$ was more positive than the reduction potential for OH/OH^- ($+2.40$ V vs. NHE) [12] and the VB potential of $LaNiO_3$ was more positive than the reduction potential for OH/OH^- ($+2.40$ V vs. NHE) and H_2O/OH ($+2.72$ V vs. NHE) [12]. The h^+ can also be involved in degradation reactions due to its own strong oxidizability. As a result, O_2^- and OH produced and h^+ can decompose NOR into small molecules and eventually into CO_2 , H_2O and NH_3 . The analysis above could be validated by radical quenching experiments. Consequently, it can be ascertained that 3-ALG ternary component photocatalyst adheres to a dual Z-scheme photogenerated charge transfer system. In this system, photogenerated holes and electrons are separated and migrated efficiently, while the photocatalyst retains a high oxidation-reduction capacity for contaminants.

3. Materials and Methods

3.1. Synthesis of $g-C_3N_4$ Nanosheets

We synthesized $g-C_3N_4$ nanosheets based on the method described in the previous report [21]. Firstly, 10 g of melamine was placed in a covered crucible and heated at 550 °C for 4 h with a heating rate of 2 °C per minute in air. The bulk $g-C_3N_4$ achieved was ground into powder, subsequently put into a crucible without a lid and heated at 520 °C for another 2 h in air with a heating rate of 2 °C per minute to get $g-C_3N_4$ nanosheets.

3.2. Synthesis of $LaNiO_3$ Nanospheres

Typically, 1 mmol $La(NO_3)_3 \cdot 6H_2O$, 1 mmol $Ni(NO_3)_2 \cdot 6H_2O$ and 5 mmol citric acid were dissolved in 200 mL deionized water with magnetic stirring for 2 h to achieve light green solution. The solution was poured into a 250 mL Teflon-lined stainless autoclave, heated at 180 °C for 12 h. The precipitate collected was washed with deionized water and ethanol for several times after cooling to room temperature and dried at 80 °C for 24 h and calcinated at 800 °C for 2 h in air to achieve pure $LaNiO_3$ nanospheres.

3.3. Synthesis of $AgBr$ Nanoparticles

$AgNO_3$ and KBr (1 mmol) were dissolved in 300 mL deionized water in dark with magnetic stirring for 30 min, washed by deionized water and ethanol for several times and dried at 60 °C for 12 h. $AgBr$ nanoparticles were obtained.

3.4. Synthesis of LG Hybrid

$LaNiO_3$ nanospheres (0.3 g) and 1 g $g-C_3N_4$ nanosheets were mixed in 30 mL deionized water with magnetic stirring and ultrasonic vibration for 2 h. The resulting mixture was dried at 80 °C for 24 h to remove the remaining water, and calcinated in the air at 300 °C for 2 h. Then $LaNiO_3$ nanospheres were successfully assembled on the surface of $g-C_3N_4$ nanosheets, the sample obtained was marked as LG.

3.5. Synthesis of ALG Photocatalysts

Typically, 0.03 g $AgBr$, 0.3 g $LaNiO_3$, and 1 g $g-C_3N_4$ was poured into 20 mL deionized water with magnetic stirring for 2 h, and endured for 12 h with ultrasonic vibration at room temperature. The mixture was dried at 80 °C for 24 h. After calcination in air for 3 h at 300 °C, we obtained ALG composites. By controlling the mass ratio of $AgBr$, the catalysts with a load of 1%, 3% and 5% of $AgBr$ were accurately prepared and named as 1-ALG, 3-ALG and 5-ALG, respectively.

3.6. Characterization of Samples

We used XRD (Shimadzu, LabX-6000) to investigate the crystal structures of samples obtained. The chemical bonds on the surface of photocatalysts were examined by FTIR (Bruker, Vertex70, Karlsruhe, Germany). SEM (Hitachi, S-4800, Tokyo, Japan) and TEM (Tecnai, G2 F30, Hillsboro, OR, USA) were employed to detect the morphology of the samples. The element composition was characterized by XPS (VG-Multilab, 200, Madison, GA, USA). Nitrogen adsorption-desorption isotherms were conducted at 77 K using an ASAP 2460 surface area and porosity analyzer at liquid nitrogen temperature. We employed PL (Shimadzu, RF-6000, Kyoto, Japan) and UV-vis DRS (JASCO, UV-2600, Tokyo, Japan) to examine the photogenerated charge separation efficiency and optical absorption capacity. The transit photocurrent and electrochemical impedance spectroscopy (EIS) were conducted on an electrochemical workstation (Chenhua Instrument Corp, CHI 660E, Shanghai, China).

3.7. Photodegradation Measurements

The photocatalytic performance of as-obtained samples was tested by degradation experiments of NOR in aqueous solution. The visible-light source was provided by a 500 W xenon lamp equipped with a 420 nm cut filter.

Typically, 20 mg of the sample as-obtained was added into 100 mL 20 mg/L NOR solution with magnetic stirring in a quartz tube reactor with a water circulation facility. Before light irradiation, the mixture suspension was remained in the dark for 30 min to reach the adsorption-desorption equilibrium between photocatalysts and degradation product. During the photodegradation process, 10 mL of the suspension was withdrawn and centrifuged to remove the photocatalyst each 20 min. The absorbance of the supernatant was examined at a wavelength of 280 nm. The photodegradation ratio for NOR was tested by the formula below:

$$\eta = (1 - C_t/C_0) \times 100\% \quad (1)$$

where η is the photodegradation ratio for NOR, C_t and C_0 represent the initial and remaining NOR in aqueous solution, t is the light irradiation time, respectively.

4. Conclusions

In conclusion, a novel ternary dual Z-scheme AgBr/LaNiO₃/g-C₃N₄ photocatalyst was prepared via a facile ultrasound-assisted hydrothermal method. The introduction of AgBr promoted the optical absorption capacity of the heterojunction and made it possible for the metallic Ag to participate in degradation. Such a heterojunction possessed a high specific surface area of 65.39 m²/g, which can absorb more undecomposed molecules and provide photocatalytic reaction with more active sites. Metallic Ag involved in the reaction acting as the electron-holes transfer media to enhance the separation of charge pairs. A possible dual Z-scheme reaction mechanism was proposed, in which the light absorption and charge pairs separation were promoted. This novel ALG exhibited excellent photocatalytic performance for norfloxacin (NOR), 92% of NOR was degraded over 3-ALG within 120 min. In addition, ALG possessed remarkable stability and reusability. This study provided a feasible way to establish the ternary component dual Z-scheme g-C₃N₄-based photocatalyst and a possible method for photocatalysis in the decomposition of antibiotic-like contaminants in water.

Author Contributions: Conceptualization, Z.Z.; methodology, J.Z.; writing, J.Z.; validation, J.J. and H.L. All authors have read and agreed to the published version of the manuscript.

Funding: This research received no external funding.

Conflicts of Interest: The authors declare no conflict of interest.

References

1. Chen, M.; Chu, W. Photocatalytic degradation and decomposition mechanism of fluoroquinolones norfloxacin over bismuth tungstate: Experiment and mathematic model. *Appl. Catal. B Environ.* **2015**, *168*, 175–182. [[CrossRef](#)]
2. Tang, L.; Wang, J.; Zeng, G.; Liu, Y.; Deng, Y.; Zhou, Y.; Tang, J.; Wang, J.; Guo, Z. Enhanced photocatalytic degradation of norfloxacin in aqueous Bi₂WO₆ dispersions containing nonionic surfactant under visible light irradiation. *J. Hazard. Mater.* **2016**, *306*, 295–304. [[CrossRef](#)]
3. Xu, M.; Ye, M.; Zhou, X.; Cheng, J.; Huang, C.; Wong, W.; Wang, Z.; Wang, Y.; Li, C. One-pot controllable synthesis of BiOBr/ β -Bi₂O₃ nanocomposites with enhanced photocatalytic degradation of norfloxacin under simulated solar irradiation. *J. Alloys Compd.* **2020**, *816*, 152664. [[CrossRef](#)]
4. Bai, J.; Li, Y.; Jin, P.; Wang, J.; Liu, L. Facile preparation 3D ZnS nanospheres-reduced graphene oxide composites for enhanced photodegradation of norfloxacin. *J. Alloys Compd.* **2017**, *729*, 809–815. [[CrossRef](#)]
5. Chen, L.; Zuo, X.; Yang, S.; Cai, T.; Ding, D. Rational design and synthesis of hollow Co₃O₄@Fe₂O₃ core-shell nanostructure for the catalytic degradation of norfloxacin by coupling with peroxy monosulfate. *Chem. Eng. J.* **2019**, *359*, 373–384. [[CrossRef](#)]
6. Behera, A.; Kandi, D.; Sahoo, S.; Parida, K. Construction of Isoenergetic Band Alignment between CdS QDs and CaFe₂O₄/ZnFe₂O₄ Heterojunction: A Promising Ternary Hybrid toward Norfloxacin Degradation and H₂ Energy Production. *J. Phys. Chem. C.* **2019**, *123*, 17112–17126. [[CrossRef](#)]
7. Baoum, A.A.; Amin, M.S.; Mohamed, R.M. Decoration of SnO₂ nanosheets by AgI nanoparticles driven visible light for norfloxacin degradation. *Appl. Nanosci.* **2018**, *8*, 2093–2102. [[CrossRef](#)]
8. Wang, W.C.; Li, S.; Wen, Y.Y.; Gong, M.C.; Zhang, L.; Yao, Y.L.; Chen, Y.Q. Synthesis and characterization of TiO₂/YFeO₃ and its photocatalytic oxidation of gaseous benzene. *Acta Phys.-Chim. Sin.* **2008**, *24*, 1761–1766. [[CrossRef](#)]
9. Zhang, Q.; Dandeneau, C.S.; Zhou, X.; Cao, C. ZnO nanostructures for dye-sensitized solar cells. *Adv. Mater.* **2009**, *21*, 4087–4108. [[CrossRef](#)]
10. Jourshabani, M.; Lee, B.K.; Shariatnia, Z. From Traditional Strategies to Z-scheme Configuration in Graphitic Carbon Nitride Photocatalysts: Recent Progress and Future Challenges. *Appl. Catal. B Environ.* **2020**, *276*, 119157. [[CrossRef](#)]
11. Ali, S.; Humayun, M.; Pi, W.; Yuan, Y.; Wang, M.; Khan, A.; Yue, P.; Shu, L.; Zheng, Z.; Fu, Q.; et al. Fabrication of BiFeO₃-g-C₃N₄-WO₃ Z-scheme heterojunction as highly efficient visible-light photocatalyst for water reduction and 2,4-dichlorophenol degradation: Insight mechanism. *J. Hazard. Mater.* **2020**, *397*, 122708. [[CrossRef](#)] [[PubMed](#)]
12. Xue, W.; Huang, D.; Li, J.; Zeng, G.; Deng, R.; Yang, Y.; Chen, S.; Li, Z.; Gong, X.; Li, B. Assembly of AgI nanoparticles and ultrathin g-C₃N₄ nanosheets codecorated Bi₂WO₆ direct dual Z-scheme photocatalyst: An efficient, sustainable and heterogeneous catalyst with enhanced photocatalytic performance. *Chem. Eng. J.* **2019**, *373*, 1144–1157. [[CrossRef](#)]
13. Cui, L.; Ding, X.; Wang, Y.; Shi, H.; Huang, L.; Zuo, Y.; Kang, S. Facile preparation of Z-scheme WO₃/g-C₃N₄ composite photocatalyst with enhanced photocatalytic performance under visible light. *Appl. Surf. Sci.* **2017**, *391*, 202–210. [[CrossRef](#)]
14. Akhundi, A.; Habibi-Yangjeh, A. Ternary magnetic g-C₃N₄/Fe₃O₄/AgI nanocomposites: Novel recyclable photocatalysts with enhanced activity in degradation of different pollutants under visible light. *Mater. Chem. Phys.* **2016**, *174*, 59–69. [[CrossRef](#)]
15. Xu, H.; Yan, J.; Xu, Y.; Song, Y.; Li, H.; Xia, J.; Huang, C.; Wan, H. Novel visible-light-driven AgX/graphite-like C₃N₄ (X=Br, I) hybrid materials with synergistic photocatalytic activity. *Appl. Catal. B Environ.* **2013**, *129*, 182–193. [[CrossRef](#)]
16. Jung, W.Y.; Hong, S.S. Synthesis of LaCoO₃ nanoparticles by microwave process and their photocatalytic activity under visible light irradiation. *J. Ind. Eng. Chem.* **2013**, *19*, 157–160. [[CrossRef](#)]
17. Zhang, Q.; Huang, Y.; Peng, S.; Zhang, Y.; Shen, Z.; Cao, J.J.; Ho, W.; Lee, S.C.; Pui, D.Y.H. Perovskite LaFeO₃-SrTiO₃ composite for synergistically enhanced NO removal under visible light excitation. *Appl. Catal. B Environ.* **2017**, *204*, 346–357. [[CrossRef](#)]
18. Wang, Z.; Su, B.; Xu, J.; Hou, Y.; Ding, Z. Direct Z-scheme ZnIn₂S₄/LaNiO₃ nanohybrid with enhanced photocatalytic performance for H₂ evolution. *Int. J. Hydrog. Energy* **2020**, *45*, 4113–4121. [[CrossRef](#)]

19. Yao, S.; Zheng, R.; Li, R.; Chen, Y.; Zhou, X.; Luo, J. Construction of Z-scheme LaNiO₃/SnS₂ composite for boosting visible light photodegradation of tetracycline. *J. Taiwan Inst. Chem. Eng.* **2019**, *100*, 186–193. [[CrossRef](#)]
20. Xu, J.; Sun, C.; Wang, Z.; Hou, Y.; Ding, Z.; Wang, S. Perovskite Oxide LaNiO₃ Nanoparticles for Boosting H₂ Evolution over Commercial CdS with Visible Light. *Chem.-A Eur. J.* **2018**, *24*, 18512–18517. [[CrossRef](#)]
21. Chen, C.; Zhou, J.; Geng, J.; Bao, R.; Wang, Z.; Xia, J.; Li, H. Perovskite LaNiO₃/TiO₂ step-scheme heterojunction with enhanced photocatalytic activity. *Appl. Surf. Sci.* **2020**, *503*, 144287. [[CrossRef](#)]
22. Yu, P.; Zhou, X.; Yan, Y.; Li, Z.; Zheng, T. Enhanced visible-light-driven photocatalytic disinfection using AgBr-modified g-C₃N₄ composite and its mechanism. *Colloids Surf. B Biointerfaces* **2019**, *179*, 170–179. [[CrossRef](#)] [[PubMed](#)]
23. Tang, G.; Zhang, F.; Huo, P.; Zulfiqar, S.; Xu, J.; Yan, Y.; Tang, H. Constructing novel visible-light-driven ternary photocatalyst of AgBr nanoparticles decorated 2D/2D heterojunction of g-C₃N₄/BiOBr nanosheets with remarkably enhanced photocatalytic activity for water-treatment. *Ceram. Int.* **2019**, *45*, 19197–19205. [[CrossRef](#)]
24. Yu, H.; Wang, D.; Zhao, B.; Lu, Y.; Wang, X.; Zhu, S.; Qin, W.; Huo, M. Enhanced photocatalytic degradation of tetracycline under visible light by using a ternary photocatalyst of Ag₃PO₄/AgBr/g-C₃N₄ with dual Z-scheme heterojunction. *Sep. Purif. Technol.* **2020**, *237*, 116365. [[CrossRef](#)]
25. Liu, Y.; Li, L.; Yu, Y.; Huang, J.; Song, X.; Zhang, W. Z-scheme and multipathway photoelectron migration properties of a bayberry-like structure of BiOBr/AgBr/LaPO₄ nanocomposites: Improvement of photocatalytic performance using simulated sunlight. *J. Alloys Compd.* **2020**, *821*, 153472. [[CrossRef](#)]
26. Chen, M.; Guo, C.; Hou, S.; Lv, J.; Zhang, Y.; Zhang, H.; Xu, J. A novel Z-scheme AgBr/P-g-C₃N₄ heterojunction photocatalyst: Excellent photocatalytic performance and photocatalytic mechanism for ephedrine degradation. *Appl. Catal. B Environ.* **2020**, *266*, 118614. [[CrossRef](#)]
27. Zhu, L.; Huang, D.; Ma, J.; Wu, D.; Yang, M.; Komarneni, S. Fabrication of AgBr/Ag₂CrO₄ composites for enhanced visible-light photocatalytic activity. *Ceram. Int.* **2015**, *41*, 12509–12513. [[CrossRef](#)]
28. Yan, S.C.; Li, Z.S.; Zou, Z.G. Photodegradation Performance of g-C₃N₄ Fabricated by Directly Heating Melamine. *Langmuir* **2009**, *25*, 10397–10401. [[CrossRef](#)]
29. Rida, K.; Peña, M.A.; Sastre, E.; Martínez-Arias, A. Effect of calcination temperature on structural properties and catalytic activity in oxidation reactions of LaNiO₃ perovskite prepared by Pechini method. *J. Rare Earths* **2012**, *30*, 210–216. [[CrossRef](#)]
30. He, Y.; Wang, Y.; Zhang, L.; Teng, B.; Fan, M. A new application of Z-Scheme Ag₃PO₄/g-C₃N₄ composite in converting CO₂ to fuel. *Environ. Sci. Technol.* **2014**, *49*, 649–656. [[CrossRef](#)]
31. Wang, G.; Liu, S.; He, T.; Liu, X.; Deng, Q.; Mao, Y.; Wang, S. Enhanced visible-light-driven photocatalytic activities of Bi₂Fe₄O₉/g-C₃N₄ composite photocatalysts. *Mater. Res. Bull.* **2018**, *104*, 104–111. [[CrossRef](#)]
32. Spectroscopy, O. Water content and water profiles in skin measured by FTIR and Raman spectroscopy. *Proc. SPIE* **2000**, *4162*, 39–45.
33. Zhou, X.; Chen, Y.; Li, C.; Zhang, L.; Zhang, X.; Ning, X.; Zhan, L.; Luo, J. Construction of LaNiO₃ nanoparticles modified g-C₃N₄ nanosheets for enhancing visible light photocatalytic activity towards tetracycline degradation. *Sep. Purif. Technol.* **2019**, *211*, 179–188. [[CrossRef](#)]
34. Makuła, P.; Pacia, M.; Macyk, W. How to Correctly Determine the Band Gap Energy of Modified Semiconductor Photocatalysts Based on UV-Vis Spectra. *J. Phys. Chem. Lett.* **2018**, *9*, 6814–6817. [[CrossRef](#)]
35. Azizi-Toupkanloo, H.; Karimi-Nazarabad, M.; Shakeri, M.; Eftekhari, M. Photocatalytic mineralization of hard-degradable morphine by visible light-driven Ag@g-C₃N₄ nanostructures. *Environ. Sci. Pollut. Res.* **2019**, *26*, 30941–30953. [[CrossRef](#)]
36. Du, H.; Pu, W.; Wang, Y.; Yan, K.; Feng, J.; Zhang, J.; Yang, C.; Gong, J. Synthesis of BiVO₄/WO₃ composite film for highly efficient visible light induced photoelectrocatalytic oxidation of norfloxacin. *J. Alloys Compd.* **2019**, *787*, 284–294. [[CrossRef](#)]
37. Li, J.; Han, M.; Guo, Y.; Wang, F.; Sun, C. Fabrication of FeVO₄/Fe₂TiO₅ composite catalyst and photocatalytic removal of norfloxacin. *Chem. Eng. J.* **2016**, *298*, 300–308. [[CrossRef](#)]
38. Prabavathi, S.L.; Govindan, K.; Saravanakumar, K.; Jang, A.; Muthuraj, V. Construction of heterostructure CoWO₄/g-C₃N₄ nanocomposite as an efficient visible-light photocatalyst for norfloxacin degradation. *J. Ind. Eng. Chem.* **2019**, *80*, 558–567. [[CrossRef](#)]

39. Liu, W.; Zhou, J.; Yao, J. Shuttle-like CeO₂/g-C₃N₄ composite combined with persulfate for the enhanced photocatalytic degradation of norfloxacin under visible light. *Ecotoxicol. Environ. Saf.* **2020**, *190*, 110062. [[CrossRef](#)] [[PubMed](#)]
40. Wang, J.; Tang, L.; Zeng, G.; Deng, Y.; Liu, Y.; Wang, L.; Zhou, Y.; Guo, Z.; Wang, J.; Zhang, C. Atomic scale g-C₃N₄/Bi₂WO₆ 2D/2D heterojunction with enhanced photocatalytic degradation of ibuprofen under visible light irradiation. *Appl. Catal. B Environ.* **2017**, *209*, 285–294. [[CrossRef](#)]
41. Wang, J.; Tang, L.; Zeng, G.; Deng, Y.; Dong, H.; Liu, Y.; Wang, L.; Peng, B.; Zhang, C.; Chen, F. 0D/2D interface engineering of carbon quantum dots modified Bi₂WO₆ ultrathin nanosheets with enhanced photoactivity for full spectrum light utilization and mechanism insight. *Appl. Catal. B Environ.* **2018**, *222*, 115–123. [[CrossRef](#)]
42. Hu, L.; Hu, H.; Lu, W.; Lu, Y.; Wang, S. Novel composite BiFeO₃/ZrO₂ and its high photocatalytic performance under white LED visible-light irradiation. *Mater. Res. Bull.* **2019**, *120*, 110605. [[CrossRef](#)]

Sample Availability: Samples of the compounds are available from the authors.



© 2020 by the authors. Licensee MDPI, Basel, Switzerland. This article is an open access article distributed under the terms and conditions of the Creative Commons Attribution (CC BY) license (<http://creativecommons.org/licenses/by/4.0/>).